



**UNIVERSIDAD NACIONAL AUTÓNOMA DE MÉXICO**  
**POSGRADO EN CIENCIAS FÍSICAS**  
**Óptica y Fotónica**

**TITULO QUE FALTA DEFINIR**

**PROTOCOLO DE INVESTIGACIÓN**  
**QUE PARA OPTAR POR LA:**  
**CANDIDATURA AL GRADO DE DOCTOR EN CIENCIAS (FÍSICA)**

**PRESENTA:**  
**JONATHAN ALEXIS URRUTIA ANGUIANO**

**TUTOR:**  
**DR. ALEJANDRO REYES CORONADO**  
**FACULTAD DE CIENCIAS, UNAM**

**MIEMBROS DEL COMITÉ TUTOR**  
**DR. RUBÉN RAMOS GARCÍA**  
**INSTITUTO NACIONAL DE ASTROFÍSICA, ÓPTICA Y ELECTRÓNICA**  
**DR. WOLF LUIS MOCHÁN BACKAL**  
**INSTITUTO DE CIENCIAS FÍSICAS, UNAM**

**CIUDAD DE MÉXICO, MAYO DE 2025**

# Contents

<b>Introduction</b>	<b>1</b>
<b>1 Multiple Scattering Theories: two approaches</b>	<b>7</b>
<b>2 Results and Discussion</b>	<b>13</b>
2.1 Supported and Totally Embedded Spherical Particles . . . . .	13
2.1.1 Normal Incidence . . . . .	14
<b>Conclusions</b>	<b>21</b>

# Background and Motivation

---

Optical metasurfaces are bidimensional arrays of metallic/dielectric nanostructures —known as meta-atoms— specifically tailored to behave in a way no found in nature when illuminated at specific wavelengths [1, 2]. Depending on the physical properties of the meta-atoms, that is, their composition, size, shape, orientation and distribution within the bidimensional array [1, 3], metasurfaces allow to shape at will the spatial optical response of the system [4], thus suiting them for a variety of applications in fields such as spectroscopy [1], color structuration [2], communications [4], and sensing [1, 3–6]. In the last decades, the interest in optical metasurfaces for medical applications has increased due to the need for sensitive, fast, low-cost and easy-to-use technologies [3, 5], like metasurfaces with plasmonic (metallic) meta-atoms used as contrasting agents for bioimaging [3], and as free-label biosensors returning real-time measurements [1, 5, 7].

Metasurfaces designed for biosensing typically consist of a nanostructured substrate with compatible microfluidic devices illuminated with a white light source and a light recollection system, allowing for scattering or extinction measurements, followed by a spectrometer [5, 8]. One particular kind of biosensing-aimed metasurfaces consists in plasmonic meta-atoms, exploiting their property of high confinement of light at nanometric scales, yielding an improvement in the sensitivity of various detection techniques [1]. The light confinement is the result of the meta-atom’s Localized Surface Plasmon Resonances (LSPRs) being excited at the meta-atom’s interface with its surroundings, which occurs when the electromagnetic fields couple to the free electrons of the plasmonic structure [3–5]. Since the LSPR is material and geometry dependent, a variety of plasmonic metasurfaces have been designed [7–10] —each with its own benefits and disadvantages [4, 5]— as those shown in Fig. 1, all of which are plasmonic metasurfaces consisting of gold (Au) meta-atoms on a glass substrate but with different geometries and distributions within the metasurface. For example, Feuz et al. [8] employed a short-range ordered metasurface of nanoholes to sense protein binding events in real-time [Fig. 1a)], while Kabashin et al. [7] measured changes in the refractive index of the media embedding an ordered metasurface of plasmonic nanorods [Fig. 1b)]. Metasurfaces with simpler geometries and distributions can be used for biosensing as well, as shown by Qiu et al. [9], who employed a disordered metasurface of nanospheres to detect selected DNA sequences from Severe Acute Respiratory Syndrome Coronavirus 2 (SARS-CoV-2) [Fig. 1c)], or by Svedendahl et al. [10], who sensed protein binding events with a short-range ordered metasurface of nanospheres [Fig. 1d)].

Since LSPRs are excited at frequencies that depend on the material and geometry of the nanostructures, metasurfaces of various configurations have been designed [4, 5, 7–10], as shown in Fig. ???. For example, Kabashin et al. [7] reported a biosensing metasurface con-

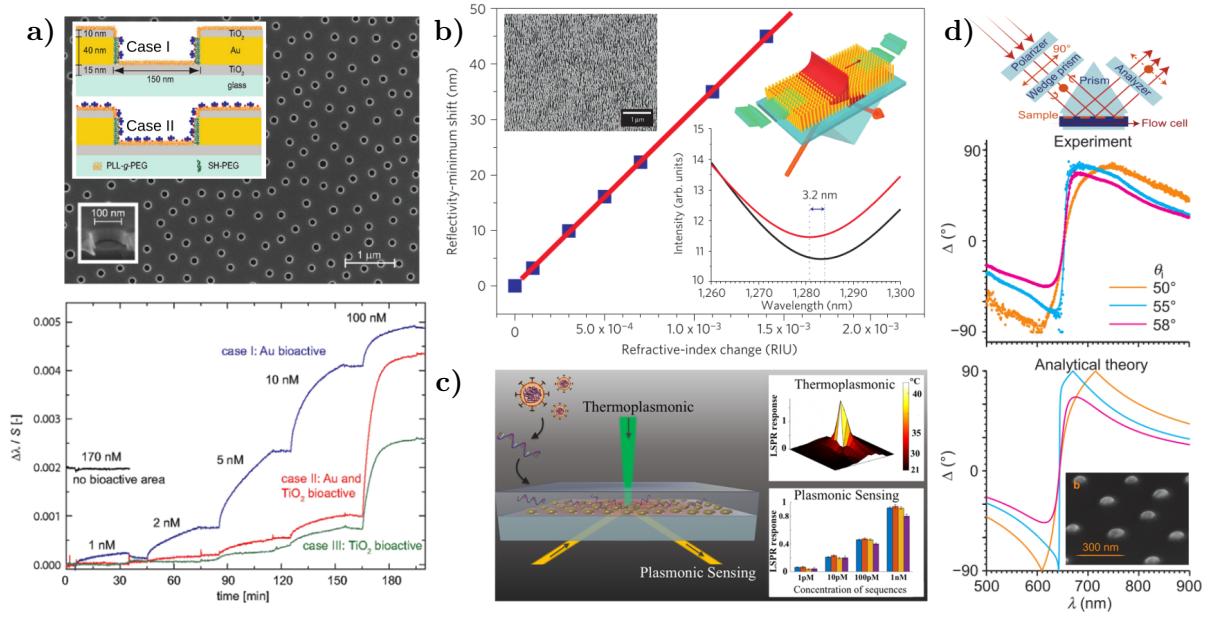


**Fig. 1:** Examples of biosensing-aimed plasmonic metasurfaces. **a)** Short-range ordered metasurface of nanoholes in a Au film [Scanning Electron Microscopy (SEM) image and meta-atom scheme] and real-time measurements of the LSPR redshift due to protein binding events; images extracted and adapted from [8]. **b)** Reflectivity minimum shift of an ordered metasurface of Au nanorods (SEM image and scheme in the inset) as a function of the refractive index change of the media embedding the metasurface; images extracted and adapted from [7]. **c)** Schematics of a disordered metasurface of Au nanospheres designed for SARS-CoV-2 detection and the LSPR response of its meta-atom: Thermoplasmonic and plasmonic sensing; image extracted from [9]. **d)** Experimental and theoretical results for the ellipsometric parameter  $\Delta$  as a function of the incident wavelength, when a short-ranged ordered metasurface of Au nanospheres (SEM image) is illuminated by a non-polarized white light as shown in the setup diagram; extracted and adapted from [10].

sisting of cylindrical gold nanoparticles (AuNPs) arranged in a square lattice [see Fig. ??]; this metasurface exhibited appropriate sensitivities for detecting changes in the refractive index of aqueous samples. Another example of the versatility and advantages of plasmonic metasurfaces for biosensing is a disordered array of spherical AuNPs on a glass substrate, used by Svedendahl et al. [10] [see Fig. ??] and Qiu et al. [9] [see Fig. ??], who detected real-time protein binding events and SARS-CoV-2 DNA sequences, respectively, by illuminating the metasurface in an internal incidence configuration and measuring the ellipsometric parameters [9, 10]. It is worth noting that with a random distribution of NPs, fabrication processes such as laser ablation [hammad\_improving\_2023] or thermal treatment known as *dewetting* [wang\_formation\_2011, cuanalo\_sensitivity\_2022] can be employed, reducing fabrication time and cost.

Metasurface design can be achieved using both analytical and numerical methods to estimate the physical characteristics that optimize their optical response for a given application. For example, the resonance wavelengths of LSPRs in ordered metasurfaces of arbitrary nanostructures have been calculated using the Finite Element Method (FEM) [8] or the Finite-Difference Time-Domain (FDTD) algorithm [12]. Additionally, the optical response of disordered metasurfaces of spherical NPs has been analytically studied using effective medium theories under the

small-particle approximation [18]. These models describe two-dimensional arrays as equivalent continuous media [bosi\_transmission\_1992].

The motivation for such a physical system arises from the collaboration between two experimental research groups<sup>1</sup> and one theoretical research group<sup>2</sup>. The experimental groups have fabricated disordered arrays of partially embedded Au nanospheres with an average radius of 12.5 nm—a potential meta-atom for biosensing-aimed metasurfaces—.

During the design stage of metasurfaces, both analytical and numerical methods can be employed to estimate the physical characteristics that optimize their optical response based on the intended application. For instance, the wavelengths at which LSPRs of ordered metasurfaces composed of arbitrary nanostructures are excited have been calculated using the Finite Element Method (FEM) [8] or the Finite-Difference Time-Domain (FDTD) algorithm [12]. Likewise, the optical response of disordered metasurfaces consisting of spherical NPs has been analytically studied using the effective medium theories under the small-particle approximation [18], where the response of two-dimensional arrays is modeled as an equivalent continuous medium [bosi\_transmission\_1992]. Examples of effective medium theories include the Dipolar Model (DM) [14, 18], the Island Film Theory (IFT) [svedendahl\_fano\_2012, 10, 13], and modifications to the Maxwell Garnett Model [7].

The characterization of a metasurface involves determining its physical properties, such as geometry, material composition, and spatial distribution of its nanostructures. One way to perform characterization is through imaging techniques such as Transmission Electron Microscopy (TEM), Scanning Electron Microscopy (SEM), and Atomic Force Microscopy (AFM). However, these methods often lead to sample damage or partial destruction. An alternative to these invasive methods is to compare optical measurements with theoretical results—obtained through numerical or analytical calculations—so that the calculated response matches the experimental data for specific metasurface parameters. For example, since the spectral position of the LSPR depends on the geometry and size of an NP, it can be identified by comparing reflectance measurements with estimated values. It is important to note that this approach requires the theoretical conditions to be reproducible in a laboratory setting.

In the case of disordered metasurfaces, effective medium theories such as DM or IFT are suitable for describing the optical response of metasurfaces composed of spherical NPs—small relative to the wavelength of illumination—perfectly positioned on a dielectric substrate [13, 14]. Both DM and IFT describe each spherical NP in the two-dimensional array as an electric dipole, allowing for relaxation of the perfect spherical geometry assumption by introducing depolarization factors, thereby extending these models to ellipsoids [15]. Additionally, DM and IFT can be applied without modification even if partial embedding of the NPs into the substrate is identified, as long as it does not exceed 12% of the NP’s volume<sup>3</sup>. Although certain geometric and embedding conditions can be relaxed while still accurately describing the behavior of disordered metasurfaces, this does not apply to all assumptions of DM or IFT, such as modeling all NPs as

---

<sup>1</sup>The Biophotonics Group and the Organic and Hybrid Semiconductor Optoelectronics Group at *Instituto Nacional de Astronomía, Óptica y Electrónica* (INAOE).

<sup>2</sup>The Nanoplasmonics Group at *Facultad de Ciencias, Universidad Nacional Autónoma de México* (UNAM).

<sup>3</sup>In my master’s thesis, FEM calculations of absorption and extinction cross-sections of a 12.5 nm radius AuNP illuminated in the visible spectrum showed that the LSPR shift relative to the case of a perfectly positioned NP was at most 5 nm when the embedding depth was one-eighth of its volume.

electric dipoles.

Both DM and IFT require the small-particle approximation, meaning a disordered meta-surface of spherical NPs must have a narrow size distribution. However, if NP synthesis is performed using physical methods such as laser ablation or *dewetting*, the size distribution may exhibit a normal distribution with significant standard deviation [hammad\_improving\_2023] or a log-normal distribution [wang\_formation\_2011, vazquez-estrada\_optical\_2014], as illustrated in Fig. ???. In such cases, some NPs within the metasurface may be large enough to require higher-order multipolar contributions beyond the dipolar approximation to accurately describe their optical response. When the small-particle approximation does not hold for a real sample, scattering theories can be used, which do not require the small-particle approximation and, unlike effective medium theories, do not describe the metasurface as an equivalent continuous film but rather provide an approximate solution to Maxwell’s equations [bosi\_transmission\_1992, 19]. A scattering theory that describes disordered arrays of spherical NPs with a given size distribution is the Coherent Scattering Model, which can be used to design and characterize metasurfaces of spherical NPs under more realistic experimental conditions. The following section presents the hypotheses, characteristics, and expressions of this model. The proposed project for the doctoral program at PCF arises from a theoretical-experimental collaboration with the Biophotonics Group—led by Prof. Rubén Ramos García—at the National Institute of Optics and Electronics (INAOE). This collaboration motivated my research topic during the PCF master’s program and now aims to extend it by introducing increasingly realistic conditions in the theoretical description of metasurfaces. The general objective of the doctoral project is to develop semi-analytical extensions to the theories mentioned in Section ???—to describe metasurfaces in a realistic biosensing environment—and to compare them with experimental results, given that the Biophotonics Group has techniques for synthesizing disordered metasurfaces of spherical gold NPs and an experimental setup for real-time reflectance spectrum measurements [cuanalo\_sensitivity\_2022].

The goals for the first year of the doctoral program are as follows:

- **Numerical implementation of the CSM considering size distribution**  
Implement the CSM expressions given by Eq. (1.12) for a size distribution determined by micrograph images. This code should account for the size correction of the dielectric function [noguez\_surface\_2007, mendoza\_herrera\_determination\_2014] of the spherical NP material to correctly compute the average size distribution.
- **Implementation of a parameter fitting method**  
Implement the gradient descent method [barzilai\_two-point\_1988] to minimize the error between optical response calculations and experimental measurements. This tool should be applicable to any theoretical model considered.
- **Comparison and evaluation of measurement schemes with the CSM**  
Evaluate and compare the method for quantifying the optical response of the metasurface when changing the refractive index of the material in contact with it. This evaluation will be conducted by comparing the figure of merit [5] for the following methods: minimum in the reflectance spectrum and phase shifts of ellipsometric parameters [9, 10].

The first goal will enable the modeling of metasurfaces like those shown in Fig. ???, allowing

the determination of optimal parameters for metasurface-based sensing applications, as well as setting a lower bound for the accuracy of the employed synthesis methods. The second goal will quantify the extent to which a model or theory describes the optical response of a metasurface while providing a tool for non-destructive metasurface characterization. The final goal focuses on analyzing the sensitivity of the metasurface and the feasibility of performing the corresponding measurements by quantifying the figure of merit of the two proposed schemes. These goals not only implement general methodologies and tools to evaluate the methods and approaches to be applied later, but also establish a path for a first publication on the characterization and performance of this type of metasurface in sensing, encompassing a theoretical-experimental analysis from synthesis to application.





# Multiple Scattering Theories: two approaches

Las teorías de esparcimiento múltiple (*Multiple Scattering Theories*, MSTs) resuelven, en el caso de esparcimiento de luz, las ecuaciones de Maxwell de forma aproximada cuando se ilumina un ensamble de partículas con una onda plana monocromática [loiko\_monolayers\_1998, 14, 19]. En particular, el Modelo de Esparcimiento Coherente (*Coherent Scattering Model*, CSM) es una MST que proporciona una expresión para los coeficientes de amplitud de reflexión y transmisión de la luz esparcida en la dirección coherente para un ensamble bidimensional desordenado de partículas esféricas [barrera\_coherent\_2003, garcia2012multiple, 19]. En esta sección se presenta de forma breve en qué consisten las MSTs y se enuncian las restricciones consideradas por el CSM.

En el esquema de las MSTs, la respuesta óptica de un arreglo desordenado de partículas arbitrarias, iluminado por una onda plana monocromática eléctrica incidente  $\mathbf{E}^{\text{inc}}(\mathbf{r}, \omega)$  con frecuencia angular  $\omega$  y dirección de propagación  $\hat{\mathbf{k}}^{\text{inc}}$ , está determinada por el campo eléctrico  $\mathbf{E}_k^{\text{exc}}(\mathbf{r}, \omega)$  que excita a  $k$ -ésima partícula, de una colección de  $N$ , y que es igual a la suma del campo eléctrico incidente y el campo eléctrico inducido  $\mathbf{E}_\ell^{\text{ind}}(\mathbf{r}, \omega)$  —el interno dentro de la partícula y el esparcido fuera de ésta— por los otros elementos del ensamble, es decir [garcia2012multiple, barrera\_coherent\_2003]

$$\mathbf{E}_k^{\text{exc}}(\mathbf{r}) = \mathbf{E}^{\text{inc}}(\mathbf{r}) + \sum_{\ell \neq k}^N \mathbf{E}_\ell^{\text{ind}}(\mathbf{r}), \quad (1.1)$$

donde se obvia la dependencia armónica. Dado que todas las partículas son excitadas por la misma interacción, el campo eléctrico inducido en la  $\ell$ -ésima partícula está dado por [garcia2012multiple, barrera\_coherent\_2003]

$$\mathbf{E}_\ell^{\text{ind}}(\mathbf{r}) = \int d^3r' \mathbb{G}(\mathbf{r}, \mathbf{r}') \int d^3r'' \mathbb{T}(\mathbf{r}' - \mathbf{r}_\ell, \mathbf{r}'' - \mathbf{r}_\ell) \mathbf{E}_\ell^{\text{exc}}(\mathbf{r}''), \quad (1.2)$$

en donde  $\mathbf{r}_\ell$  es la posición del centro de la  $\ell$ -ésima partícula,  $\mathbb{G}(\mathbf{r}, \mathbf{r}')$  es la función de Green diádica —solución a la ecuación de Helmholtz vectorial con el producto de la diádica unitaria y una delta de Dirac centrada en  $\mathbf{r}'$  como fuente [20]—,  $\mathbb{T}$  es el operador de transición, o matriz  $T$ , que relaciona de forma lineal el campo eléctrico esparcido de una partícula con el campo eléctrico que la excita [20], y las integraciones se realizan sobre un mismo volumen  $V$ , descrito por las posiciones  $\mathbf{r}'$  y  $\mathbf{r}''$ , tal que el centro  $\mathbf{r}_\ell$  de la  $\ell$ -ésima partícula se localice dentro de  $V$

[barrera\_coherent\_2003].

El campo eléctrico total  $\mathbf{E}(\mathbf{r})$  es igual a la suma de  $\mathbf{E}^{\text{inc}}(\mathbf{r})$  y las  $N$  contribuciones del campo eléctrico inducido  $\mathbf{E}_\ell^{\text{ind}}(\mathbf{r})$  en cada partícula, el cual se calcula al resolver el sistema de  $N$  ecuaciones dadas por las expresiones anteriores. Al tratar el caso de un arreglo desordenado, se calcula el promedio configuracional del campo eléctrico total  $\langle \mathbf{E}(\mathbf{r}) \rangle$ , que considera la probabilidad de ocurrencia de cada una de las combinaciones en las que pueden localizarse los centros  $\mathbf{r}_\ell$  de los elementos del ensamble [garcia2012multiple, barrera\_coherent\_2003]:

$$\langle \mathbf{E}(\mathbf{r}) \rangle = \mathbf{E}^{\text{inc}}(\mathbf{r}) + \sum_{\ell=1}^N \langle \mathbf{E}_\ell^{\text{ind}}(\mathbf{r}) \rangle = \mathbf{E}^{\text{inc}}(\mathbf{r}) + \sum_{\ell=1}^N \left( \prod_{k=1}^N \int d^3 r_k \rho(\mathbf{R}) \mathbf{E}_\ell^{\text{ind}}(\mathbf{r}) \right), \quad (1.3)$$

con  $\rho(\mathbf{R})$  la densidad de probabilidad de que el ensamble se encuentre en una configuración espacial específica dada por  $\mathbf{R} = (\mathbf{r}_1, \mathbf{r}_2, \dots, \mathbf{r}_N)^T$ . Al calcular el promedio configuracional de la Ec. (1.2) se obtiene la contribución promedio del campo eléctrico inducido en la  $\ell$ -ésima partícula, que está dada en términos de las siguientes expresiones [barrera\_coherent\_2003, garcia2012multiple]

$$\langle \mathbf{E}_\ell^{\text{ind}}(\mathbf{r}) \rangle = \int d^3 r' \mathbb{G}(\mathbf{r}, \mathbf{r}') \int d^3 r'' \int d^3 r_\ell \rho(\mathbf{r}_\ell) \mathbb{T}(\mathbf{r}' - \mathbf{r}_\ell, \mathbf{r}'' - \mathbf{r}_\ell) \langle \mathbf{E}_\ell^{\text{exc}}(\mathbf{r}'', \mathbf{R}) \rangle_\ell, \quad (1.4a)$$

$$\langle \mathbf{E}_\ell^{\text{exc}}(\mathbf{r}'', \mathbf{R}) \rangle_\ell = \prod_{\substack{k=1 \\ k \neq \ell}}^N \int d^3 r_k \rho(\mathbf{R} | \mathbf{r}_\ell) \mathbf{E}_\ell^{\text{exc}}(\mathbf{r}''), \quad (1.4b)$$

where  $\rho(\mathbf{r}_\ell)$  is the probability density of finding the center of the  $\ell$ -th particle within the volume  $V$ , and Eq. (1.4b) represents the configurational average of the excitation electric field  $\mathbf{E}_\ell^{\text{exc}}$  for the  $\ell$ -th particle, considering its fixed position in  $V$ , which is described by the conditional probability density  $\rho(\mathbf{R} | \mathbf{r}_\ell)$ . This expression can be further developed by substituting Eq. (1.1) into Eq. (1.4b) and following an analogous procedure, considering the index swaps  $k \rightarrow \ell$  and  $\ell \rightarrow m$ , yielding

$$\begin{aligned} \langle \mathbf{E}_\ell^{\text{exc}}(\mathbf{r}'', \mathbf{R}) \rangle_\ell = & \mathbf{E}^{\text{inc}}(\mathbf{r}'') + \sum_{\substack{m=1 \\ m \neq \ell}}^N \int d^3 r' \mathbb{G}(\mathbf{r}', \mathbf{r}'') \times \\ & \int d^3 r''' \int d^3 r_m \rho(\mathbf{r}_m) \mathbb{T}(\mathbf{r}' - \mathbf{r}_m, \mathbf{r}''' - \mathbf{r}_m) \langle \mathbf{E}_m^{\text{exc}}(\mathbf{r}''', \mathbf{R}) \rangle_{\ell, m}, \end{aligned} \quad (1.5a)$$

$$\langle \mathbf{E}_m^{\text{exc}}(\mathbf{r}''', \mathbf{R}) \rangle_{\ell, m} = \prod_{\substack{n=1 \\ n \neq \ell, m}}^N \int d^3 r_n \rho(\mathbf{R} | \mathbf{r}_\ell, \mathbf{r}_m) \mathbf{E}_n^{\text{exc}}(\mathbf{r}'''), \quad (1.5b)$$

where Eq. (1.5b) represents the configurational average of the excitation field  $\mathbf{E}_m^{\text{exc}}(\mathbf{r}''')$  acting on the  $m$ -th particle, considering the conditional probability density  $\rho(\mathbf{R} | \mathbf{r}_\ell, \mathbf{r}_m)$  that the system is in configuration  $\mathbf{R}$  with  $\mathbf{r}_\ell$  and  $\mathbf{r}_m$  fixed [garcia2012multiple, barrera\_coherent\_2003]. By continuing this process for all  $N$  spheres in the ensemble, a set of  $N$  equations known as the Foldy-Lax hierarchy [loiko\_monolayers\_1998] can be constructed. Solving this hierarchy enables the computation of the averaged electric field at  $\mathbf{r}$ , taking multiple scattering effects

---

**Fig. 1.1:** Diagram of the particle ensemble considered in the CSM, consisting of a collection of  $N$  identical spherical particles of radius  $a$  whose centers are randomly located within the integration volume  $V$ : an infinite film centered at the plane  $z = 0$  and of thickness  $d$ , which tends to zero to reproduce the case of a two-dimensional array. The system, embedded in a dielectric matrix, is illuminated by a monochromatic plane wave incident on the film at an angle  $\theta$ .

into account. The hierarchical equations can be truncated at different orders, reducing them to invertible systems of equations by applying approximations to how multiple scattering excites the elements of the ensemble.

To truncate the Foldy-Lax hierarchy and determine the total averaged electric field, the CSM imposes two approximations at different orders. First, the Single Scattering Approximation (SSA) is considered, reducing the Foldy-Lax hierarchy to a single equation to be solved by neglecting multiple scattering effects [barrera\_coherent\_2003]. Specifically, in the SSA, Eq. (1.4b) is equated to the incident electric field  $\mathbf{E}^{\text{inc}}(\mathbf{r})$  [loiko\_monolayers\_1998, garcia2012multiple]. The second approximation in the CSM is the Quasi-Crystalline Approximation (QSA), where the Foldy-Lax hierarchy is rewritten as a system of two equations by assuming that the configurational average for cases with one and two fixed particles is approximately equal, meaning that Eqs. (1.4b) and (1.5) are set equal [loiko\_monolayers\_1998, barrera\_coherent\_2003]. While the SSA is suitable for dilute disordered arrays, as it disregards multiple scattering, the QSA adapts to denser ensembles—up to a coverage fraction of 60% [loiko\_monolayers\_1998]—because, under this condition, the average with two fixed particles does not significantly differ from the average with one fixed particle due to the presence of the remaining particles [barrera\_coherent\_2003].

Once the approximation orders have been determined to truncate the Foldy-Lax hierarchy, the CSM introduces a series of assumptions about the particle ensemble to solve the resulting system of equations for each approximation. In particular, the CSM considers that the particle ensemble consists of  $N \gg 1$  identical spherical particles of radius  $a$ —immersed in a dielectric medium called the matrix—whose centers  $\mathbf{r}_\ell$  are within the integration volume  $V$ , which consists of an infinite film of thickness  $d$  centered at  $z = 0$ , with a uniform probability density  $\rho(\mathbf{r}_\ell) = 1/V$ , and assumes that the volume  $V_\ell$  of each sphere is negligible compared to  $V$  [barrera\_coherent\_2003]; a schematic of the system is shown in Fig. 1.1. Under these assumptions, the electric field induced by the ensemble particles in the SSA can be computed by substituting in Eq. (1.4) the dyadic Green function  $\mathbb{G}$  with its plane wave representation and performing the configurational average, along with the limit  $d \rightarrow 0$  to consider the case of a two-dimensional array [barrera\_coherent\_2003]. This procedure results in

$$\langle \mathbf{E}_{\text{SSA}}^{\text{ind}}(\mathbf{r}) \rangle = \begin{cases} -\alpha S_j(\pi - 2\theta) \exp(i\mathbf{k}_{\text{coh}}^{\text{r}} \cdot \mathbf{r}) \mathbf{E}^{\text{inc}}(\mathbf{r}), & z > 0, \\ -\alpha S(0) \exp(i\mathbf{k}_{\text{coh}}^{\text{t}} \cdot \mathbf{r}) \mathbf{E}^{\text{inc}}(\mathbf{r}), & z < 0, \end{cases} \quad \text{with} \quad \alpha = \frac{2\Theta}{x^2 \cos \theta}, \quad (1.6)$$

where  $\theta$  is the incidence angle at which the incident plane wave illuminates the two-dimensional array,  $S_j(\vartheta)$  are the elements of the Mie scattering matrix [21]—which depend on the refractive index of the matrix, the sphere, and its size—evaluated at  $\vartheta$ , with  $j = 1$  for  $s$ -polarization and  $j = 2$  for  $p$ -polarization. The term  $\Theta$  corresponds to the coverage fraction of the array, and  $x = k^{\text{ind}} a$  is the size parameter with  $k^{\text{ind}}$  being the magnitude of the incident field wave vector propagating

in the matrix [barrera\_coherent\_2003, garcia2012multiple]. The elements  $S_j(\vartheta)$  are evaluated at  $\vartheta = \pi - 2\theta$  and  $\vartheta = 0$  as they correspond to the coherent scattering directions given by the law of reflection and Snell's law, respectively. From Eq. (1.6), it is shown that under the SSA, the two-dimensional array of spherical particles scatters light primarily in coherent directions, as the diffuse components interfere destructively [barrera\_coherent\_2003]. Consequently, reflection  $r_{\text{SSA}}^{(j)}$  and transmission  $t_{\text{SSA}}^{(j)}$  amplitude coefficients can be defined for the two-dimensional array similarly to the Fresnel coefficients, given by

$$r_{\text{SSA}}^{(j)}(\theta) = -\alpha S_j(\pi - 2\theta), \quad \text{and} \quad t_{\text{SSA}}^{(j)}(\theta) = 1 - \alpha S(0). \quad (1.7)$$

In the case of the QSA, the system of equations to be solved consists of Eqs. (1.4) and (1.5), considering that Eqs. (1.4b) and (1.5b) are equal. To solve this system of equations, the ensemble is assumed to have the same characteristics as in the SSA case and additionally that the surroundings of each sphere are identical on average [garcia2012multiple]. Therefore, the system of equations can be solved by proposing the *ansatz*

$$\langle \mathbf{E}_\ell^{\text{exc}}(\mathbf{r}) \rangle_\ell = \mathbf{E}_\text{r}^{\text{exc}}(\mathbf{r}) \exp(i\mathbf{k}_\text{coh}^\text{r} \cdot \mathbf{r}) + \mathbf{E}_\text{t}^{\text{exc}}(\mathbf{r}) \exp(i\mathbf{k}_\text{coh}^\text{t} \cdot \mathbf{r}) \quad (1.8)$$

that is, in the CSM, it is assumed that  $\langle \mathbf{E}_\ell^{\text{exc}}(\mathbf{r}) \rangle_\ell$  consists of a contribution from an electric field propagating in the coherent reflection direction, denoted as  $\mathbf{E}_\text{r}^{\text{exc}}$ , and another in the transmission direction, denoted by  $\mathbf{E}_\text{t}^{\text{exc}}$  [garcia2012multiple]. These coherent contributions behave according to the SSA [Eq. (1.6)], so each will have a reflected and transmitted component. The sum of these contributions determines the induced electric field under the QSA. Solving the system of equations and substituting in Eq. (1.9), the amplitude coefficients of reflection  $r_{\text{CSM}}^{(j)}$  and transmission  $t_{\text{CSM}}^{(j)}$  can be defined, considering multiple scattering [garcia2012multiple, barrera\_coherent\_2003]. These coherent contributions behave according to the SSA [Eq. (1.6)], so each of them will have a reflected and a transmitted component. The sum of these contributions determines the induced electric field under the QSA, whose expression is

$$\langle \mathbf{E}_{\text{QSA}}^{\text{ind}}(\mathbf{r}) \rangle = \begin{cases} -\alpha \left( S_j(0) \|\mathbf{E}_\text{r}^{\text{exc}}(\mathbf{r})\| + S(\pi - 2\theta) \|\mathbf{E}_\text{t}^{\text{exc}}(\mathbf{r})\| \right) \exp(i\mathbf{k}_\text{coh}^\text{r} \cdot \mathbf{r}) \hat{\mathbf{E}}^{\text{inc}}, & z > 0, \\ -\alpha \left( S_j(\pi - 2\theta) \|\mathbf{E}_\text{r}^{\text{exc}}(\mathbf{r})\| + S(0) \|\mathbf{E}_\text{t}^{\text{exc}}(\mathbf{r})\| \right) \exp(i\mathbf{k}_\text{coh}^\text{t} \cdot \mathbf{r}) \hat{\mathbf{E}}^{\text{inc}}, & z < 0, \end{cases} \quad (1.9)$$

where  $\hat{\mathbf{E}}^{\text{inc}}$  indicates the polarization of the incident electric field. Since in the QSA the expressions of Eq. (1.5) are equal for the electric field exciting a particle, then the contributions of the induced field in the coherent direction satisfy [garcia2012multiple]

$$\mathbf{E}_\text{r}^{\text{exc}}(\mathbf{r}) = -\frac{\alpha}{2} \left( S_j(0) \|\mathbf{E}_\text{r}^{\text{exc}}(\mathbf{r})\| + S(\pi - 2\theta) \|\mathbf{E}_\text{t}^{\text{exc}}(\mathbf{r})\| \right) \hat{\mathbf{E}}^{\text{inc}}, \quad (1.10a)$$

$$\mathbf{E}_\text{t}^{\text{exc}}(\mathbf{r}) = \mathbf{E}^{\text{inc}}(\mathbf{r}) - \frac{\alpha}{2} \left( S_j(\pi - 2\theta) \|\mathbf{E}_\text{r}^{\text{exc}}\| + S(0) \|\mathbf{E}_\text{t}^{\text{exc}}(\mathbf{r})\| \right) \hat{\mathbf{E}}^{\text{inc}}. \quad (1.10b)$$

Solving the system of equations for  $\mathbf{E}_\text{r}^{\text{exc}}(\mathbf{r})$  and  $\mathbf{E}_\text{t}^{\text{exc}}(\mathbf{r})$  shown in Eq. (1.10), and substituting them in Eq. (1.9), expressions for the reflection  $r_{\text{CSM}}^{(j)}$  and transmission  $t_{\text{CSM}}^{(j)}$  amplitude coefficients are defined, considering multiple scattering. These expressions are [garcia2012multiple,

---

**barrera\_coherent\_2003]**

$$r_{\text{CSM}}^{(j)}(\theta) = \frac{-\alpha S_j(\pi - 2\theta)}{1 + \alpha S(0) + \frac{1}{4}\alpha^2 [S^2(0) - S_j^2(\pi - 2\theta)]}, \quad (1.11a)$$

$$t_{\text{CSM}}^{(j)}(\theta) = \frac{1 - \frac{1}{4}\alpha^2 [S^2(0) - S_j^2(\pi - 2\theta)]}{1 + \alpha S(0) + \frac{1}{4}\alpha^2 [S^2(0) - S_j^2(\pi - 2\theta)]}, \quad (1.11b)$$

where  $j = 1$  for  $s$ -polarization and  $j = 2$  for  $p$ -polarization. The assumption that spherical particles are identical, imposed in both the SSA and QSA, can be relaxed if the radius  $a$  of the particles follows a size distribution density  $\rho(a)$  and the field exciting each sphere is identical for all, except for a phase difference of  $\pm 2ik_z^{\text{inc}}a$  caused by size variation [**vazquez-estrada\_optical\_2014**]. In this case, the average over the particle radius  $a$  is computed in Eq. (1.10), incorporating the phase difference by multiplying the right-hand side of Eq. (1.10) by  $\exp(\pm 2ik_z^{\text{inc}}a)$ —with  $k_z^{\text{ind}} = k^{\text{ind}} \cos \theta$ , where the positive sign corresponds to the reflected contribution and the negative to the transmitted one. Following the analogous procedure described earlier, the reflection and transmission amplitude coefficients considering size polydispersity in the two-dimensional array are given by [**vazquez-estrada\_optical\_2014**].

$$r_{\text{CSM}}^{(j)}(\theta) = \frac{-\beta_+^{(j)}(\theta)}{1 + \beta_F + \frac{1}{4}[\beta_F^2 - \beta_+^{(j)}(\theta)\beta_-^{(j)}(\theta)]}, \quad (1.12a)$$

$$t_{\text{CSM}}^{(j)}(\theta) = \frac{1 - \frac{1}{4}[\beta_F^2 - \beta_+^{(j)}(\theta)\beta_-^{(j)}(\theta)]}{1 + \beta_F + \frac{1}{4}[\beta_F^2 - \beta_+^{(j)}(\theta)\beta_-^{(j)}(\theta)]}, \quad (1.12b)$$

where

$$\beta_F(\theta) = \eta \int_0^\infty \rho(a) S(0) da \quad \text{y} \quad \beta_\pm^{(j)}(\theta) = \eta \int_0^\infty \rho(a) S_j(\pi - 2\theta) \exp(\pm 2ik_z^{\text{inc}}a) da, \quad (1.13)$$

with  $\eta = 2\Theta/(x_0^2 \cos \theta)$  and where  $x_0 = k^{\text{ind}}a_0$  is the size parameter of a sphere with radius  $a_0$ , which is the most probable value according to the size distribution density  $\rho(a)$ .

The expressions in Eq. (1.12) allow describing the response of a disordered metasurface of spherical NPs under conditions close to experimental ones by introducing the presence of a substrate. To achieve this, multiple reflections between the substrate-matrix interface and the matrix-metasurface interface are considered, assuming that the latter responds according to Eq. (1.12) when separated from the substrate by a distance  $\Delta \rightarrow 0$  [**vazquez-estrada\_optical\_2014**]. In particular, to compare the theoretical response with reflectance measurements in an internal incidence scheme, the amplitude reflection coefficient of the entire system (metasurface with substrate) is given by [**vazquez-estrada\_optical\_2014**]

$$r^{(j)}(\theta_i) = \frac{r_{\text{sm}}^{(j)}(\theta_i) + r_{\text{CSM}}^{(j)}(\theta_t)}{1 + r_{\text{sm}}^{(j)}(\theta_i)r_{\text{CSM}}^{(j)}(\theta_t)}, \quad (1.14)$$

where  $r_{\text{sm}}$  is the Fresnel reflection coefficient between the substrate and the matrix for  $s$  ( $p$ )

## 1. MULTIPLE SCATTERING THEORIES: TWO APPROACHES

---

polarization if  $j = 1$  ( $j = 2$ ), and where  $\theta_i$  is the angle of incidence of the plane wave illuminating the interface between the substrate and the matrix, and  $\theta_t$  is the transmission angle upon crossing this interface and thus the angle at which it illuminates the metasurface.

# Results and Discussion

## 2.1 Supported and Totally Embedded Spherical Particles

To compare the optical response of a NP in the presence of a substrate with that of a NP in a totally homogeneous environment, let us first analyze the spectral response given by the Mie Theory when the matrix and the size of the NP varies. In Fig. 2.1 it is shown the wavelength of resonance  $\lambda_{\text{res}}$ , that is, the wavelength at which the scattering (orange) and extinction (black) efficiencies are maximized, as a function of the radius  $a$  of a AuNP embedded in a matrix of air [Fig. 2.1a)] and of glass [Fig. 2.1b)], with a refractive index of  $n_{\text{m}} = 1$  and  $n_{\text{m}} = 1.5$ , respectively, and as a function of the refractive index of the matrix  $n_{\text{m}}$  for a AuNP with a radius of  $a = 12.5$  nm [Fig. 2.1c)] and with a radius of  $a = 50$  nm [Fig. 2.1d)]. For the optical response of the AuNP it was employed the experimental data as reported by Johnson and Christy [27] (filled circles) and by considering a size correction —see Appendix ??— to it (empty circles).

From the results shown in Fig. 2.1 it can be seen that the wavelength of resonance  $\lambda_{\text{res}}$  for the extinction, considering the bulk dielectric function for Au (filled circles), is smaller than that of the scattering and that the distance between them decreases as either the size of the AuNP or the refractive index of the matrix increases. This behavior arises from a redshift of  $\lambda_{\text{res}}$  for increasing values of  $a$  and  $n_{\text{m}}$  and it shows that, for particles small compared to the wavelength of the incident light in the matrix, the main contribution to the extinction of light is due to absorption processes and as the size of the AuNP grows, the extinction is dominated by its other contribution: the scattering, as discussed in Section ?? and supported by Eq. (??). The redshift of  $\lambda_{\text{res}}$  can also be observed when considering a size corrected dielectric function (empty circles). Remarkably, for values of radius  $\lesssim 15/n_{\text{m}}$  there is a blueshift of  $\lambda_{\text{res}}$ , as it can be seen in Figs. 2.1a) and 2.1b), which is a consequence of a greater imaginary part of the dielectric function for the AuNP due to the size correction. On the other hand, an increase in  $n_{\text{m}}$  for a fixed radius presents only redshifts either with or without a size corrected dielectric function [see Figs. 2.1c) and 2.1d)].

The spectral behavior of the scattering and extinction of light due to a spherical NP summarized in Fig. 2.1 was calculated by assuming a homogeneous medium (the matrix) where the NP is embedded and thus allowing the direction of the illuminating plane wave to be arbitrary, yet yielding the same results. In the following Sections, the homogeneity of the surroundings of the NP is substituted by two semiinfinite media and thus modifying the optical response of the

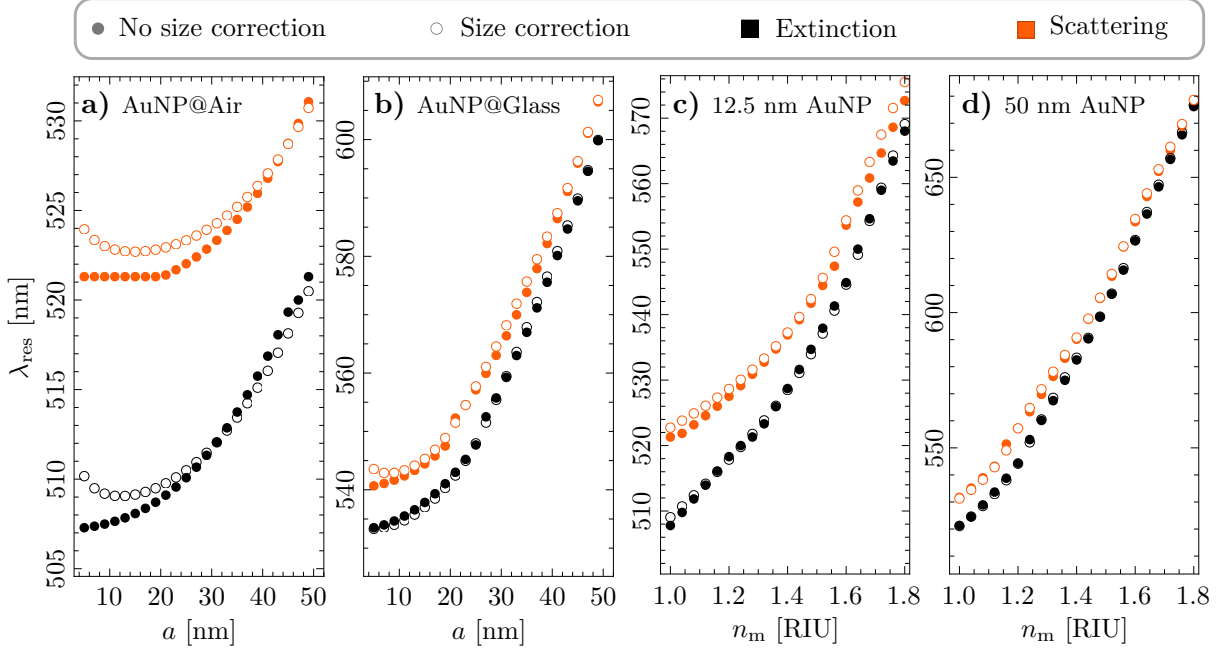


**Fig. 2.1:** Resonance wavelength  $\lambda_{\text{res}}$  of the scattering (orange) and extinction (black) efficiencies of a AuNP as a function of the NP’s radius when embedded **a)** in air ( $n_m = 1$ ) and **b)** in glass ( $n_m = 1.5$ ), and as a function of the refractive index of the matrix  $n_m$  for a AuNP of radius **c)** 12.5 nm and **d)** 50 nm, using the dielectric function for gold as reported by Johnson and Christy [27] (filled circles) and considering a size correction to it (empty circles).

system depending on how it is illuminated.

### 2.1.1 Normal Incidence

The problem of scattering and absorption of light by single spherical NP embedded in a matrix, with refractive index  $n_m$ , illuminated by a plane wave with wavelength  $\lambda$  and traveling in the  $\mathbf{k}^i$  direction, has spherical symmetry, which was exploited to develop the Mie Theory as explained in Section ???. If a substrate, with refractive index  $n_s$ , is considered and the NP is located right above or below the interface—without crossing the substrate-matrix interface—, there are four combinations in which the system can be excited since the NP can be either embedded in the substrate or supported on it, and it can be illuminated either in an external—from the matrix to the substrate—or in an internal—from the substrate to matrix— configuration, as shown in Fig. 2.2a), where the following cases are depicted: Embedded-External (EE), Embedded-Internal (EI), Supported-External (SE) and Supported-Internal (SI). In the presence of the substrate, the electric field illuminating the AuNP is not the incoming plane wave but the sum of it with the reflected electric field (EI and SE) or the transmitted electric field (EE and SI), both of which can be calculated analytically through Fresnel’s reflection and transmission amplitude coefficients, as discussed in Appendix ??.

In Figs. 2.2b) and 2.2c) the absorption  $Q_{\text{abs}}$  and scattering  $Q_{\text{sca}}$  efficiencies are shown, respectively, as a function of  $\lambda$  for a AuNP of radius  $a = 12.5$  nm in the Embedded-External



(black), Embedded-Internal (orange), Supported-External (blue) and Supported-Internal (light orange) configurations; the green shaded regions correspond to the values between the two limiting cases given by the Mie theory: the AuNP embedded in air (lower boundary) and embedded in glass (upper boundary). The magenta markers correspond to the values of the efficiencies evaluated at the wavelength of resonance considering the presence of a substrate while the cyan markers correspond to the efficiencies at the resonance wavelength for the Mie-limiting cases.

From the results shown in Figs. 2.2b) and 2.2c), it can be seen that both the absorption and scattering efficiencies of the four spatial configurations are of the same order of magnitude as the Mie-limiting cases and, even more, the values of the efficiencies for the embedded AuNP (black and orange lines) lie very close to the Mie-limiting case of the AuNP in glass (upper boundary of the green shaded region) and the same behavior is observed for the supported AuNP (blue and light orange lines) and the Mie-limiting case of a AuNP embedded in air (lower boundary of the green shaded region). The presence of a substrate yields an overall enhancement and damping of the scattering and the absorption efficiencies relative to the isolated NP, which depend on the illumination of the system since  $Q_{\text{abs}}$  and  $Q_{\text{sca}}$  are inversely proportional to the refractive index of the medium of incidence [Ecs. (??) and (??)]: If the system is illuminated in an external configuration, the obtained efficiencies are slightly decreased relative to the Mie-limiting case as it can be seen from the black and blue curves, which correspond to the EE and SE cases; on the other hand, the calculated efficiencies for the internal illuminated cases, that is for EI (orange) and SI (light orange), are enhanced relative to the Mie-limiting cases.

Another effect of the substrate in the optical response of the system is a slightly spectral shift of the excitation wavelength of the scattering and absorption efficiencies, which depends on the medium where the AuNP is located. For example, in Figs. 2.2b) and 2.2c) the wavelength of

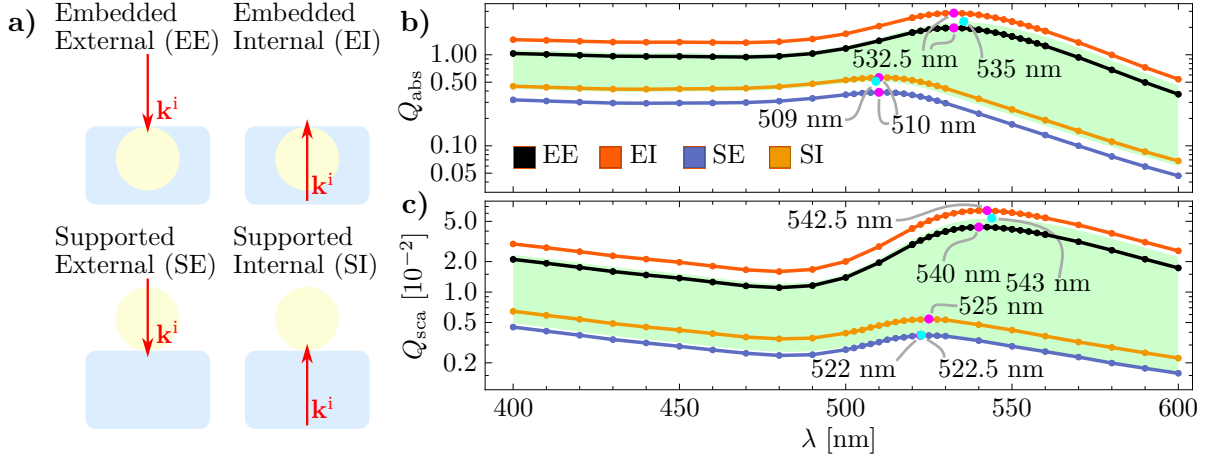


**Fig. 2.2:** a) Schematics of a AuNP embedded (E) in [supported (S) on] a glass substrate ( $n_s = 1.5$ ) forming a planar interface with an air matrix ( $n_m = 1$ ) and illuminated by a plane wave traveling normally to the air-glass interface in an external (E) and in an internal (I) configuration. b) Absorption  $Q_{\text{abs}}$  and c) scattering  $Q_{\text{sca}}$  efficiencies of a 12.5 nm AuNP as a function of the wavelength  $\lambda$  of the illuminating plane wave in different spatial configurations: EE (black), EI (orange), SE (blue) and SI (light orange). The green shaded region shows the two Mie-limiting cases of a AuNP embedded in air and in glass; the magenta (AuNP and substrate) and cyan (Mie-limiting) markers correspond to the efficiencies evaluated at the wavelength of resonance for each case.

## 2. RESULTS AND DISCUSSION

---

resonance for both the absorption and the scattering efficiencies (magenta markers) are redshifted  $\sim 1$  nm, relative to the Mie-limiting case (cyan markers), for the AuNP supported on the substrate (blue and light orange curves) and blueshifted  $\sim 2$  nm for the embedded AuNP (black and orange curves). These spectral shifts can be understood by considering the AuNPs as electric point dipoles parallel to the interface—an assumption consistent with the near-field distribution in the Mie-limiting cases and with the radiation patterns (see Figs. ?? and ??)—and their interaction with the image electric point dipoles induced within the substrate [11]. Both the dipoles induced in the AuNP and the image dipoles are parallel to the interface but its strength differs by a factor of  $A_{\text{dip}} = (\sqrt{n_j} - \sqrt{n_i})/(\sqrt{n_j} + \sqrt{n_i})$  [14], where  $n_j$  is the refractive index of the medium where the real dipole (the AuNP) is located and  $n_i$  of the medium where the image dipole is induced. If the AuNP is embedded in the substrate, then  $A_{\text{dip}} > 0$  meaning that the induced dipole is parallel to the real dipole, which is a more energetic configuration that yields the spectral blueshift of the resonance. Conversely, if the AuNP is supported on the substrate then  $A_{\text{dip}} < 0$  and the induced dipole is antiparallel to the real dipole, leading to a less energetic configuration and to the redshift observed in Figs. 2.2b) and 2.2c).

The absorption and scattering efficiencies are integral quantities which describe the global behavior of the induced electric field  $\mathbf{E}^{\text{ind}}$ , which corresponds to the internal electric field  $\mathbf{E}^{\text{int}}$  inside the AuNP and to the scattered electric field  $\mathbf{E}^{\text{sca}}$  outside of it. The distribution of  $\mathbf{E}^{\text{ind}}$ , for a fixed wavelength, is studied in two spatial regimes: the far- and the near-field. To analyze the optical response in the first regime, the radiation patterns of the AuNP are obtained numerically by plotting the magnitude of the scattered electric field in the far-field regime<sup>1</sup>  $\mathbf{E}_{\text{far}}^{\text{sca}}$  as a function of the angle relative to the normal direction to the interface. In Figs. 2.3 and 2.4, it is shown the radiation patterns of the embedded and the supported AuNP, respectively, for several values of the wavelength  $\lambda$  of the incident plane wave, as well as considering an illumination of the system in an [a) and b)] external and in an [c) and d)] internal configuration; additionally, it is considered that the incident electric field is totally [a) and c)] parallel to the scattering plane  $\mathbf{E}_{\parallel}^{\text{i}}$  and [b) and d)] perpendicular to the scattering plane  $\mathbf{E}_{\perp}^{\text{i}}$ .

The radiation patterns of both the embedded and the supported AuNP follow the same trend independently of the illuminating wavelength  $\lambda$  but the amplitude is modulated by the scattering efficiencies shown in Fig. 2.2c). For example, in the EE and EI cases (Fig. 2.3) the scattered electric field (in the far-field) decreases its amplitude as the wavelength increases from 400 nm to 480 nm (black, orange and blue curves) and from 550 nm to 600 nm, while it increases from 485 nm to 542 nm, near the wavelength of resonance for the scattering efficiency, see Fig. 2.2c). Similarly, for the SE and SI cases the amplitude of the far-field is modulated by its scattering efficiency as it can be seen from comparing the radiation patterns in Fig. 2.4 at 400 nm (black), 480 nm (blue) and 527 nm (purple), with the value of  $Q_{\text{sca}}$  at those wavelengths corresponding to a global maximum, a global minimum and a local maximum at the wavelength

---

<sup>1</sup>The FEM returns the induced electric field by a scatterer in a neighborhood around it and there is no guarantee that the returned electric field, even at the boundaries of the volume where the FEM simulation is performed, corresponds to the far-field regime. To calculate the radiation pattern from the obtained induced electric field, COMSOL Multiphysics™ Ver. 5.4 employs the Stratton-Chu formula [28], which is a near-field to far-field transformation that propagates the known electric near-field over a mathematical surface surrounding all the scatterers to an arbitrary point [29]. The Stratton-Chu formula is obtained by employing the vectorial generalization of the Green's second identity with the electric and magnetic near-fields and the Green's function to the scalar Helmholtz equation multiplied by a normal vector to the integration surface [30].

of resonance, respectively [see Fig. 2.2c)].

The shape of the radiation pattern of a 12.5 nm AuNP in the presence of a substrate, either embedded or supported, resembles that of the isolated 12.5 nm AuNP discussed in Section ?? [see Fig. ??] in that it follows a two-lobe and a one-lobe pattern depending on the orientation of  $\mathbf{E}^i$  relative to the scattering plane. If the incident electric field is parallel to the scattering plane, a two-lobe pattern aligned to the direction  $\mathbf{k}^i$  of the incident —and transmitted— plane wave arises as it can be seen in the Figs. 2.3a) and 2.3c) for the EE case, and Figs. 2.4a) and 2.4c) for the EI scenario. Contrastingly, when the incident electric field is perpendicular to the scattering plane, the one-lobe pattern can be identified [see Figs. 2.3b) and 2.3d) (SE), and 2.4b) and 2.4d) (SI)]. By comparing the Mie-limiting radiation pattern (see Fig. ??) with the radiation patterns considering a substrate, the later loses the polar symmetry observed in the Mie-limiting case. In particular, the amplitude of  $\mathbf{E}_{\text{far}}^{\text{sca}}$  is larger when evaluated at the medium of incidence than at medium of transmission; this asymmetry is observed for both illuminating configurations

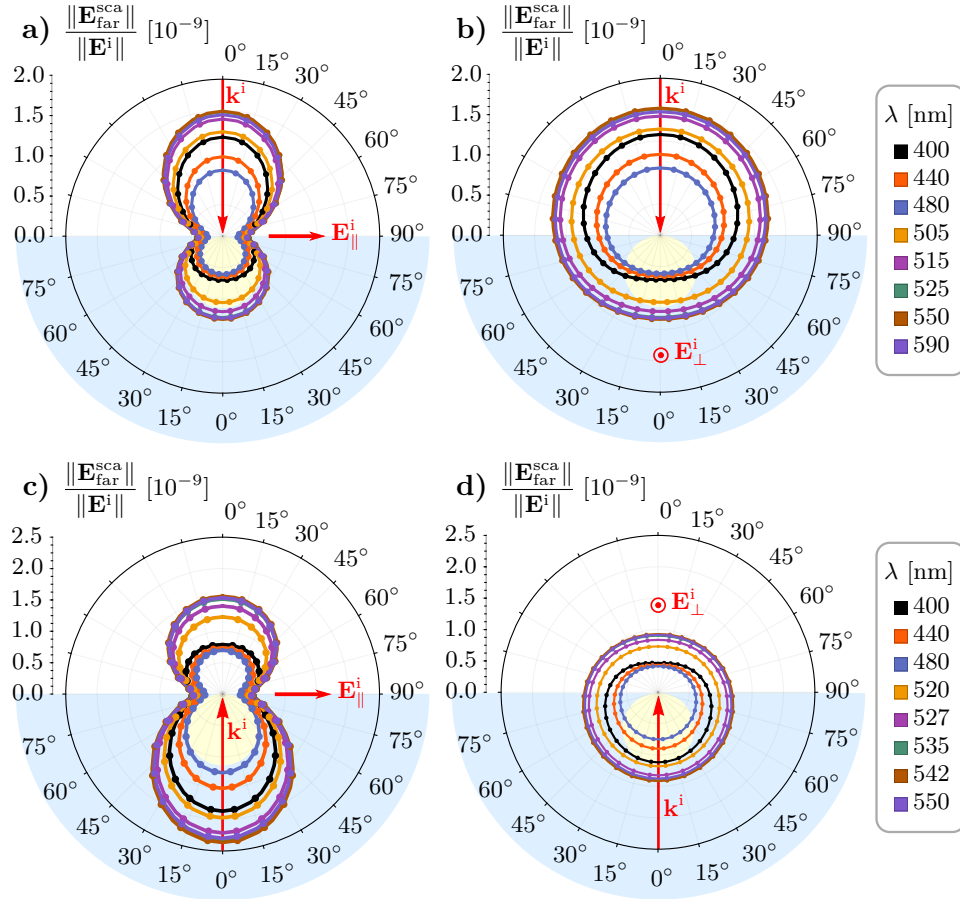


**Fig. 2.3:** Radiation patterns of a AuNP (light yellow) of radius  $a = 12.5$  nm, embedded in a substrate (light blue) and illuminated by an electric plane wave  $\mathbf{E}^i$  with a wavelength  $\lambda$ , traveling in the  $\mathbf{k}^i$  direction normal to the interface between the substrate ( $n_s = 1.5$ ) and the matrix ( $n_m = 1$ ). The radiation patterns consider the illumination of the system **a,b**) in an external and **c,d**) in an internal configuration, and with an incident electric field **a,c**)  $\mathbf{E}_{\parallel}^i$  parallel to the scattering plane and **b,d**)  $\mathbf{E}_{\perp}^i$  perpendicular to it.

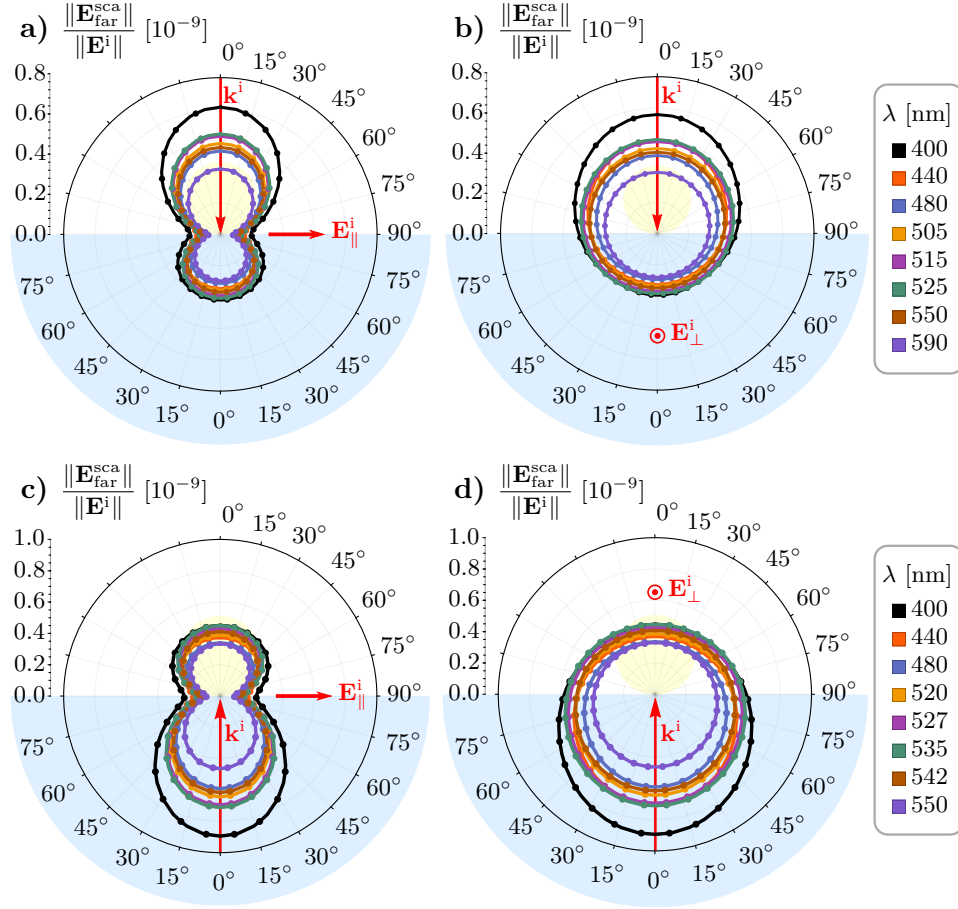


**Fig. 2.4:** Radiation patterns of a AuNP (light yellow) of radius  $a = 12.5$  nm, supported on a substrate (light blue) and illuminated by an electric plane wave  $\mathbf{E}^i$  with a wavelength  $\lambda$ , traveling in the  $\mathbf{k}^i$  direction normal to the interface between the substrate ( $n_s = 1.5$ ) and the matrix ( $n_m = 1$ ). The radiation patterns consider the illumination of the system a,b) in an external and c,d) in an internal configuration, and with an incident electric field a,c)  $\mathbf{E}^i_{||}$  parallel to the scattering plane and b,d)  $\mathbf{E}^i_{\perp}$  perpendicular to it.

(external and internal) and it does not depend on whether the AuNP is supported or embedded. Rather, the spatial configuration of the system determines the overall value of the far-field: when the AuNP is embedded, the far-field amplitude is greater by a factor of 2.5 than when the AuNP is supported—see the axis scale in Figs. 2.3 and 2.4—; this phenomenon is a consequence of the two following physical mechanisms. The first one is the substrate having a greater refractive index than the matrix, thus making the optical response of the 12.5 nm AuNP as that of a larger NP—but still small compared to the illuminating wavelength—, as in the Mie-limiting case. The second mechanism is the relative alignment of the electric point dipole induced within the AuNP—small particle approximation to the AuNP—and the induced electric dipole due to the interface, which is parallel when the AuNP is embedded into the substrate and antiparallel when supported on it, thus leading to a more energetic configuration when the AuNP is located inside the substrate than inside the matrix.

The radiation pattern, an optical property observed in the far-field regime, is a mani-

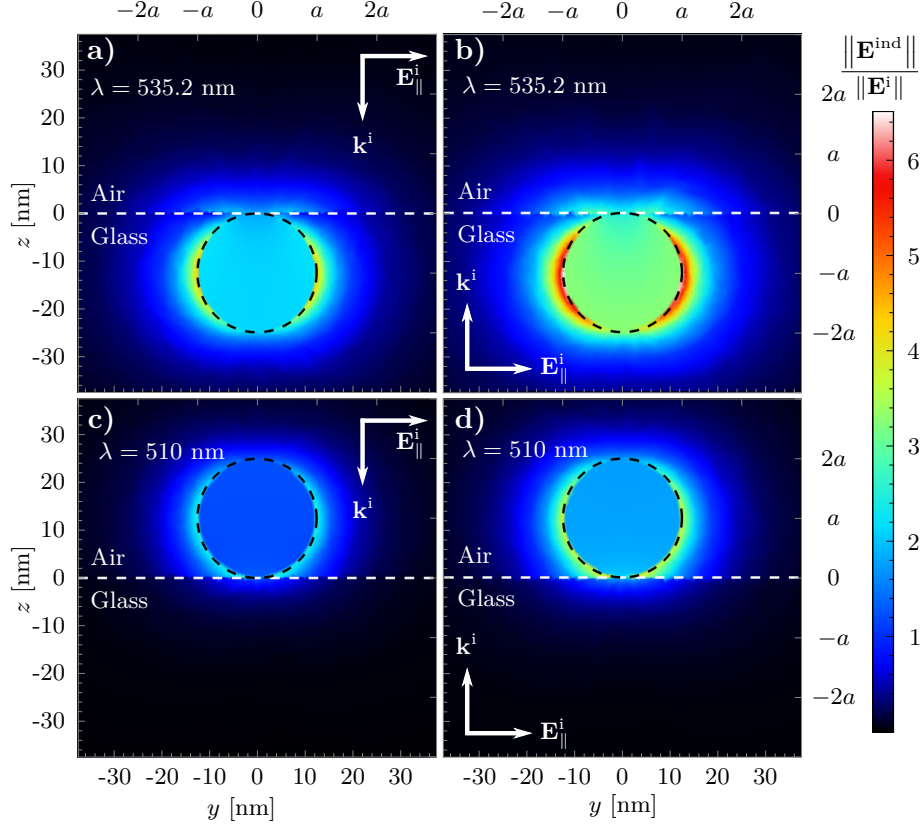


**Fig. 2.5:** Magnitude of the electric field induced  $\mathbf{E}^{\text{ind}}$  by a 12.5 nm AuNP (dashed black lines) illuminated by an incident electric plane wave  $\mathbf{E}^i$  traveling in the  $\mathbf{k}^i$  direction perpendicular to the interface (dashed white lines) between an air matrix ( $n_m = 1$ ) and a glass substrate ( $n_s = 1.5$ ) when the AuNP is **a,b**) embedded in the glass substrate and **c,d**) supported on it; the system is illuminated **a,c**) in an external and **b,d**) in an internal configuration at the resonance wavelength for the absorption efficiency.

festation of the near-field spatial distribution —see the footnote on page 16— which can be calculated numerically through the FEM for a AuNP of radius  $a = 12.5$  nm. The scattered electric field in the far-field regime of a AuNP embedded or supported [Figs. 2.3 and 2.4] share some characteristics with the radiated field of an isolated AuNP (Mie-limiting case), and thus it should be for the near-field. In Fig. 2.5 it is shown the magnitude of the induced electric field  $\mathbf{E}^{\text{ind}}$  when the AuNP is illuminated by a  $y$ -polarized incident electric field  $\mathbf{E}^i$  traveling in the  $\mathbf{k}^i$  direction, perpendicular to the interface between air and glass; the induced electric field is evaluated at the scattering plane  $x = 0$ , that is, the incident electric field has only a parallel contribution  $\mathbf{E}^i_{\parallel}$  to the scattering plane. The wavelength  $\lambda$  of the incoming plane wave is  $\lambda = 535.2$  nm for an embedded AuNP either illuminated externally [Fig. 2.5a)] or internally [Fig. 2.5b)] and  $\lambda = 510$  nm for a supported AuNP either illuminated externally [Fig. 2.5c)] or internally [Fig. 2.5d)], which correspond to the wavelengths of the Localized Surface Plasmon Resonance (LSPR), that is, at the wavelength of maximum absorption.

The spatial distribution of the near-field shown in Fig. 2.5 is consistent with the description and explanation of both the absorption and scattering efficiencies [Figs. 2.2b) and 2.2c)] and the radiation patterns of the embedded [Fig. 2.3] and the supported [Fig. 2.4] AuNP. The induced

## 2. RESULTS AND DISCUSSION

---

electric field is, in general, stronger when the AuNP is embedded in the substrate than when it is supported on it, as can be seen in the magnitude of the hotspots around the AuNP: reddish regions in Figs. 2.5a) and 2.5b) and bluish in Figs. 2.5c) and 2.5d). These hotspots also verify that at the resonance wavelength, the main contribution to the electric fields is due to an electric dipolar moment since the characteristic two-lobe distribution of the near-field can be easily identified nevertheless, the lobes are not horizontally aligned to the AuNP's equator but farther from the substrate for the embedded AuNP and closer to it for the supported AuNP, as if the induced dipole—in the small particle approximation, where the AuNP is treated as an electric point dipole—is parallel (perpendicular) to the dipolar moment induced in the AuNP when it is embedded in (supported on) the substrate, as discussed above.

Throughout this Section, the optical properties of a 12.5 nm AuNP on the presence of a substrate considering four configurations were studied: the AuNP either embedded or supported and the system illuminated from under the substrate or from above. The choice of normal incidence to the system allowed the obtained results to be compared with the Mie-limiting case, which lead to the identification of similarities and differences among the four configurations. The differences in the optical response are associated to the broken symmetry due to the two semiinfinite media now considered [11], while the similarities arise since the system is always illuminated by a plane wave independently of the choice of the medium of incidence, yielding a mostly dipolar electric field. Therefore, in the next Section the oblique incidence case is addressed only when the AuNP is supported and illuminated in the internal configuration, since it is the only case with a different type illumination to the system: an evanescent wave for incidence angles above the critical angle  $\theta_c = \arcsin(n_m/n_s)$  [26].

# Conclusions

---

In this thesis, the optical properties of a spherical gold nanoparticle (AuNP) of radius  $a = 12.5$  nm, partially embedded in an air matrix and in a glass substrate, was studied as a function of its embedding degree, characterized by the incrustation parameter  $h/a$  —with  $h$  the position of the center of the AuNP relative to the planar air-glass interface—. By means of the Finite Element Method —implemented in the commercial software COMSOL Multiphysics™ Ver. 5.4— the absorption and scattering efficiencies, the radiation pattern and the spatial distribution of the induced electric field of the partially embedded 12.5 nm AuNP were calculated when the AuNP was illuminated by an electromagnetic plane wave traveling at an oblique direction, with a defined polarization state; all numerical results were compared with the Mie-limiting cases calculated analytically, consisting in a 12.5 nm AuNP embedded in an infinite matrix of air, and an infinite matrix of glass. From the preformed calculations, it was observed that the 12.5 nm AuNP with partial embedding can be described by a mainly dipolar contribution, that its coupling with the incident light and the spatial distribution of the electric field enhancement on its surface can be tuned depending on the embedding of the AuNP and its illumination conditions, and that the optical response is maximized if the system is illuminated with an evanescent wave at an angle of incidence near the critical angle. More specifically, from the preformed calculations the following can be concluded:

- **The optical response of a single partially embedded AuNP can be described by a mainly dipolar contribution.**

The absorption and scattering efficiencies present only one global maximum in the visible spectrum, at which the spatial distribution of the electric field enhancement and its radiation pattern resemble that of an electric point dipole. This behavior can be extended to other materials of the matrix, the substrate and the nanosphere (of any size) as long as the scattering contribution to the extinction of light is small compared to the absorption contribution.

- **There is a smooth transition between the two Mie-limiting cases as the nanosphere is partially embedded into the substrate.**

The wavelength of resonance of the absorption and scattering efficiencies of the partially embedded nanosphere is localized in between the two Mie-limiting cases, which consist in the nanosphere embedded in an infinite media (either the matrix or the substrate). Additionally, the wavelength of resonance is redshifted from the resonance wavelength of the matrix Mie-limiting case to the resonance wavelength of the substrate Mie-limiting case, and this redshift is different for an  $s$  or for a  $p$  polarized incident electric field.



- **The optical response of the nanosphere resembles that of a supported (totally embedded) nanosphere if at most one eighth of its volume is partially embedded in the substrate (matrix).**

The supported and totally embedded nanosphere are the extreme cases of the partially embedded nanosphere when the sphere is tangential to the matrix-substrate interface. The absorption and scattering efficiencies of the partially embedded nanospheres, for both polarizations, are enhanced and redshifted in the same trend as the supported and totally embedded spheres as the angle of incidence of the incident light changes if at most one eighth of the nanosphere crossed the interface.

- **The optical properties of the partially embedded nanospheres are maximized if illuminated at an angle of incidence near the critical angle.**

For any incrustation parameter and polarization state, the magnitude of the scattering and absorption efficiencies is enhanced—for all wavelengths in the visible spectrum—as the angle of incidence grows from zero to the critical angle, and they start to diminish for angles of incidence above the critical angle. This behavior is due to the effect of an evanescent wave illuminating the system above the interface, whose penetration depth is maximum at the critical angle.

- **The wavelength of resonance and the electric field spatial distribution of the partially embedded nanospheres for  $s$  polarized illumination do not depend on the angle of incidence while they do for  $p$  polarized illumination.**

On the one hand, for  $s$  polarization, the redshift of the resonance wavelength as the nanosphere is buried into the substrate, is the same for all angles of incidence and the electric field at the resonance wavelength is enhanced in two hotspots aligned parallel to the interface and on the surface of the nanosphere in the substrate side of the system. On the other hand, for  $p$  polarization, the redshift of the resonance wavelength is different for each angle of incidence. For example, near the critical angle, the redshift is appreciable if more than half of the nanosphere is buried into the substrate, while for normal incidence the behavior is equivalent to the  $s$  polarization case. On the spatial distribution, one hotspot is located in the matrix and other in the substrate, and their alignment is determined by the transmitted electric field; in particular, for angles above the critical angle, the hotspots are aligned perpendicular to the substrate.

Finally, it can be concluded that the optical properties of a partially embedded spherical AuNP of radius 12.5 nm, with at most one eighth of its volume buried into the substrate, is suited for interactions with elements in the matrix under internal illumination. If the system is illuminated with a  $p$  polarized incident electromagnetic plane wave traveling at an angle  $\theta_i \gtrsim \theta_c$ , the system is optimized to interact with its surroundings above the substrate since the optical response is maximized in the matrix. Therefore, partially embedded spherical AuNPs are strong candidates for meta-atoms conforming a disordered biosensing-aimed-metasurface.



# Bibliography

---

- [1] S. A. Khan, N. Z. Khan, Y. Xie, M. T. Abbas, M. Rauf, I. Mehmood, M. Runowski, S. Agathopoulos, and J. Zhu. Optical sensing by metamaterials and metasurfaces: from physics to biomolecule detection. *Advanced Optical Materials*, **10**(18):2200500, 2022. DOI: [10.1002/adom.202200500](https://doi.org/10.1002/adom.202200500) (cited on page 1).
- [2] A. K. González-Alcalde and A. Reyes-Coronado. Large angle-independent structural colors based on all-dielectric random metasurfaces. *Optics Communications*, **475**:126289, 2020. DOI: [10.1016/j.optcom.2020.126289](https://doi.org/10.1016/j.optcom.2020.126289) (cited on page 1).
- [3] M. Kim, J. Lee, and J. Nam. Plasmonic photothermal nanoparticles for biomedical applications. *Advanced Science*, **6**(17):1900471, 2019. DOI: [10.1002/advs.201900471](https://doi.org/10.1002/advs.201900471). (Visited on 10/27/2022) (cited on page 1).
- [4] H.-T. Chen, A. J. Taylor, and N. Yu. A review of metasurfaces: physics and applications. *Reports on Progress in Physics*, **79**(7):076401, 2016. DOI: [10.1088/0034-4885/79/7/076401](https://doi.org/10.1088/0034-4885/79/7/076401) (cited on page 1).
- [5] M.-C. Estevez, M. A. Otte, B. Sepulveda, and L. M. Lechuga. Trends and challenges of refractometric nanoplasmonic biosensors: a review. *Analytica Chimica Acta*, **806**:55–73, 2014. DOI: [10.1016/j.aca.2013.10.048](https://doi.org/10.1016/j.aca.2013.10.048) (cited on pages 1, 4).
- [6] P. K. Jain, X. Huang, I. H. El-Sayed, and M. A. El-Sayed. Noble metals on the nanoscale: optical and photothermal properties and some applications in imaging, sensing, biology, and medicine. *Accounts of Chemical Research*, **41**(12):1578–1586, 2008. DOI: [10.1021/ar7002804](https://doi.org/10.1021/ar7002804) (cited on page 1).
- [7] A. V. Kabashin, P. Evans, S. Pastkovsky, W. Hendren, G. A. Wurtz, R. Atkinson, R. Pollard, V. A. Podolskiy, and A. V. Zayats. Plasmonic nanorod metamaterials for biosensing. *Nature Materials*, **8**(11):867–871, 2009. DOI: [10.1038/nmat2546](https://doi.org/10.1038/nmat2546) (cited on pages 1–3).
- [8] L. Feuz, P. Jönsson, M. P. Jonsson, and F. Höök. Improving the limit of detection of nanoscale sensors by directed binding to high-sensitivity areas. *ACS Nano*, **4**(4):2167–2177, 2010. DOI: [10.1021/nm901457f](https://doi.org/10.1021/nm901457f) (cited on pages 1–3).
- [9] G. Qiu, Z. Gai, Y. Tao, J. Schmitt, G. A. Kullak-Ublick, and J. Wang. Dual-functional plasmonic photothermal biosensors for highly accurate severe acute respiratory syndrome coronavirus 2 detection. *ACS Nano*, **14**(5):5268–5277, 2020. DOI: [10.1021/acsnano.0c02439](https://doi.org/10.1021/acsnano.0c02439) (cited on pages 1, 2, 4).
- [10] M. Svedendahl, R. Verre, and M. Käll. Refractometric biosensing based on optical phase flips in sparse and short-range-ordered nanoplasmonic layers. *Light: Science & Applications*, **3**(11):e220–e220, 2014. DOI: [10.1038/lsa.2014.101](https://doi.org/10.1038/lsa.2014.101) (cited on pages 1–4).

- [11] X. Meng, T. Shibayama, R. Yu, J. Ishioka, and S. Watanabe. Anisotropic surroundings effects on photo absorption of partially embedded au nanospheroids in silica glass substrate. *AIP Adv*, **5**(2):027112, 2015. DOI: [10.1063/1.4908010](https://doi.org/10.1063/1.4908010) (cited on pages [16](#), [20](#)).
- [12] G. Qiu, S. P. Ng, and C. M. L. Wu. Differential phase-detecting localized surface plasmon resonance sensor with self-assembly gold nano-islands. *Optics Letters*, **40**(9):1924, 2015. DOI: [10.1364/OL.40.001924](https://doi.org/10.1364/OL.40.001924) (cited on pages [2](#), [3](#)).
- [13] D. Bedeaux and J. Vlieger. *Optical properties of surfaces*. Imperial College Press, London, 2nd edition, 2004. 450 pages. ISBN: 978-1-86094-450-5 (cited on page [3](#)).
- [14] R. G. Barrera, M. del Castillo-Mussot, G. Monsivais, P. Villaseor, and W. L. Mochán. Optical properties of two-dimensional disordered systems on a substrate. *Phys. Rev. B*, **43**(17):13819–13826, 1991. DOI: [10.1103/PhysRevB.43.13819](https://doi.org/10.1103/PhysRevB.43.13819) (cited on pages [3](#), [7](#), [16](#)).
- [15] A. Sihvola. *Electromagnetic Mixing Formulas and Applications*. Electronic Waves. The Institution of Engineering and Technology, 2008. ISBN: 978-0-85296-772-0 (cited on page [3](#)).
- [16] T. Oates, H. Wormeester, and H. Arwin. Characterization of plasmonic effects in thin films and metamaterials using spectroscopic ellipsometry. *Progress in Surface Science*, **86**(11):328–376, 2011. DOI: [10.1016/j.progsurf.2011.08.004](https://doi.org/10.1016/j.progsurf.2011.08.004).
- [17] R. S. Moirangthem, M. T. Yaseen, P.-K. Wei, J.-Y. Cheng, and Y.-C. Chang. Enhanced localized plasmonic detections using partially-embedded gold nanoparticles and ellipsometric measurements. *Biomedical Optics Express*, **3**(5):899, 2012. DOI: [10.1364/B0E.3.000899](https://doi.org/10.1364/B0E.3.000899).
- [18] A. Reyes-Coronado, G. Pirruccio, A. K. González-Alcalde, J. A. Urrutia-Anguiano, A. J. Polanco-Mendoza, G. Morales-Luna, O. Vázquez-Estrada, A. Rodríguez-Gómez, A. Issa, S. Jradi, et al. Enhancement of light absorption by leaky modes in a random plasmonic metasurface. *The Journal of Physical Chemistry C*, **126**(6):3163–3170, 2022. DOI: <https://doi.org/10.1021/acs.jpcc.1c08325> (cited on page [3](#)).
- [19] A. Reyes-Coronado, G. Morales-Luna, O. Vázquez-Estrada, A. García-Valenzuela, and R. G. Barrera. Analytical modeling of optical reflectivity of random plasmonic nano-monolayers. *Optics Express*, **9594**:6697–6706, 2018. DOI: [10.1364/OE.26.012660](https://doi.org/10.1364/OE.26.012660) (cited on pages [4](#), [7](#)).
- [20] L. Tsang, J. A. Kong, and K.-H. Ding. *Scattering of Electromagnetic Waves: Theories and Applications*. John Wiley & Sons, Inc., New York, USA, 2000. ISBN: 978-0-471-22428-0 978-0-471-38799-2. DOI: [10.1002/0471224286](https://doi.org/10.1002/0471224286) (cited on page [7](#)).
- [21] C. F. Bohren and D. R. Huffman. *Absorption and Scattering of Light by Small Particles*. Wiley Science Paperbak Series. John Wiley & Sons, 1st edition, 1983. ISBN: 0-471-029340-7 (cited on page [9](#)).
- [22] J. D. Jackson. *Classical electrodynamics*. Wiley, New York, 3rd edition, 1999. ISBN: 978-0-471-30932-1.
- [23] M. Pellarin, C. Bonnet, J. Lermé, F. Perrier, J. Laverdant, M.-A. Lebeault, S. Hermelin, M. Hillenkamp, M. Broyer, and E. Cottancin. Forward and Backward Extinction Measurements on a Single Supported Nanoparticle: Implications of the Generalized Optical Theorem. *The Journal of Physical Chemistry C*, **123**(24):15217–15229, 2019. DOI: [10.1021/acs.jpcc.9b03245](https://doi.org/10.1021/acs.jpcc.9b03245).
- [24] R. G. Newton. Optical theorem and beyond. *American Journal of Physics*, **44**(7):639–642, 1976. DOI: [10.1119/1.10324](https://doi.org/10.1119/1.10324).
- [25] A. V. Krasavin, P. Segovia, R. Dubrovka, N. Olivier, G. A. Wurtz, P. Ginzburg, and A. V. Zayats. Generalization of the optical theorem: experimental proof for radially polarized beams. *Light: Science & Applications*, **7**(1):36, 2018. DOI: [10.1038/s41377-018-0025-x](https://doi.org/10.1038/s41377-018-0025-x).

- [26] M. Born and W. Emil. *Principle of Optics: Electromagnetic Theory of Propagation, Interference and Diffraction of Light*. Cambridge University Press, New York, USA, 7th edition, 1999. ISBN: 0-521-64222-1 (cited on page 20).
- [27] P. B. Johnson and R. W. Christy. Optical Constants of the Noble Metals. *Physical Review B*, **6**(12):4370–4379, 1972. DOI: [10.1103/PhysRevB.6.4370](https://doi.org/10.1103/PhysRevB.6.4370) (cited on pages 13, 14).
- [28] COMSOL Multiphysics™ Ver. 6.0. *Wave Optics Module User’s Guide*. <https://doc.comsol.com/5.4/doc/com.comsol.help.woptics/WaveOpticsModuleUsersGuide.pdf>. COMSOL AB. Stockholm, Sweden., 2021 (cited on page 16).
- [29] N. V. Anyutin, K. I. Kurbatov, I. M. Malay, and M. A. Ozerov. Algorithm for transforming antenna electromagnetic near-field measured on spherical surface into far-field based on direct calculation of Stratton and Chu formulas. *Radioelectronics and Communications Systems*, **62**(3):109–118, 2019. DOI: [10.3103/S0735272719030026](https://doi.org/10.3103/S0735272719030026) (cited on page 16).
- [30] J. A. Stratton and L. J. Chu. Diffraction theory of electromagnetic waves. *Physical Review*, **56**(1):99–107, 1939. DOI: [10.1103/PhysRev.56.99](https://doi.org/10.1103/PhysRev.56.99) (cited on page 16).